DR. RICARDO A. MATUTE (Orcid ID : 0000-0002-0644-3799)

Article type : Special Issue Research Article

SPECIAL ISSUE RESEARCH ARTICLE

The Keto-Enol Tautomerism of Biliverdin in Bacteriophytochrome: Could it Explain the Bathochromic Shift in the Pfr Form?†

Nery Villegas-Escobar[1] and Ricardo A. Matute[1, 2, *]

[1)]Centro Integrativo de Biología y Química Aplicada (CIBQA), Universidad Bernardo O'Higgins, Santiago 8370854, Chile

[2)]Division of Chemistry and Chemical Engineering, California Institute of Technology, Pasadena, California 91125, USA.

*Corresponding author e-mail: rmatute@caltech.edu (Ricardo A. Matute)

†This article is part of a Special Issue commemorating the XIV ELAFOT Conference held from November 11th to 14th, 2019 in Viña del Mar, Chile.

This article has been accepted for publication and undergone full peer review but has not been through the copyediting, typesetting, pagination and proofreading process, which may lead to differences between this version and the Version of Record. Please cite this article as doi: 10.1111/PHP.13341

ABSTRACT

Phytochromes are ubiquitous photoreceptors found in plants, eukaryotic algae, bacteria, and fungi. Particularly, when bacteriophytochrome is irradiated with light, a *Z-to-E* (photo)isomerization takes place in the biliverdin chromophore as part of the Pr to Pfr conversion. This photoisomerization is concomitant with a bathochromic shift in the Q-band. Based on experimental evidence we studied a possible keto-enol tautomerization of BV, as an alternative reaction channel after its photoisomerization. In this contribution, the non-catalyzed and water-assisted reaction pathways for the lactam-lactim interconversion through consecutive keto-enol tautomerization of a model BV species were studied deeply. It was found that in the absence of water molecules the proton transfer reaction is unable to take place at normal conditions, due to large activation energies and the endothermic formation of lactim-derivatives prevents its occurrence. However, when a water

molecule assists the process by catalyzing the proton transfer reaction, the activation free energy lowers considerably. The drastic lowering in the activation energy for the keto-enol tautomerism is due to the stabilization of the water moiety through hydrogen bonds along the reaction coordinate. The absorption spectra were computed for all tautomers. It was found that the UV-Visible absorption bands are in reasonable agreement with the experimental data. Our results suggest that although the keto-enol equilibrium is likely favoring the lactam tautomer, the equilibrium could eventually be shifted in favor of the lactim, as it has been reported to occur in the dark reversion mechanism of bathy phytochromes.

INTRODUCTION

Phytochromes are biological photoswitches in which a tetrapyrrole structure acts as the chromophore, switching between the physiologically inactive and active forms, namely the Pr and Pfr forms, respectively. These photoreceptors can be found in different life entities, encompassing eukaryotic algae, flowering plants, and cyanobacteria.[1–10]. These systems are biologically interesting since they can absorb and emit light in the near-infrared region, opening new developments in photochemical applications, even in biological environments due to their non-toxic character.

Albeit there are many types of phytochromes, the so-called canonical phytochromes exhibit a three-domain arrangement (PAS–GAF–PHY). Furthermore, the chromophore can vary from biliverdin (BV), phytochromobilin (PΦB), phycocyanobilin (PCB), to phycoviolobilin (PVB). The BV chromophore is shown in Fig. 1(a). Particularly, phytochromes that use BV show a conserved Cys N-terminal in the PAS domain, in contrast with the ones that utilize PCB or PΦB which have a conserved Cys in the GAF domain[12–15]. Relevant to this study is the fact that water molecules are found in the chromophore binding pocket, forming a network of hydrogen bonds, able to exchange water molecules with the exterior of the chromophore pocket, as shown in Fig. 1(b). The BV chromophore is generally found in nonoxygenic bacteria (also known as bacteriophytochromes or BphPs), the PΦB chromophore can be found in flowering plants, whereas the PCB chromophore is usually found in phytochromes of cyanobacteria (e.g., Cph1). In the present work, we studied the BV chromophore in the Pfr form of BphP. In UV-Vis spectra, this BV chromophore absorbs at around 700nm and 755 nm, in the Pr and Pfr forms, respectively[16].

<Figure 1>

<Figure 2>

These kinds of photoreceptors are known for showing a great photochromicity. In Fig.2, a general photophysical cycle in bacteriophytochromes is shown. The red-absorbing parental form, Pr, is converted upon excitation into the far-red-absorbing photoproduct (Pfr) through the formation of a metastable intermediate Lumi-R (Fig. 2). It is worth noting that in plant phytochromes the photoactivated state corresponds to Pfr, while for the bacterial ones it can vary from Pfr (prototypical phytochromes) to Pr (bathy phytochromes)[17]. This conversion takes place through photo-

isomerization of the tetrapyrrole chromophore at the C15=C16 double bond between ring C and ring D, which produces a bathochromic shift in the absorbance spectrum (see Fig. 1(c)). Particularly, we are interested in prototypical phytochromes, in which the photoisomerization converts the *15Z* conformer into a *15E* photoproduct. After photoisomerization, it is believed that noticeable conformational changes in the chromophore pocket take place, together with the reorganization of a network made of water molecules connecting the inner and outer space. Some studies suggest that the *Z-to-E* isomerization takes place in the Pr* state within a few picoseconds[18–21]. In addition, back conversion of the signaling Pfr state can be converted into the dark state Pr with intermediate formation of a meta-stable Lumi-F intermediate (see diagram in Fig. 2). For further details in the photochemical cycle in phytochromes, the reader is referred to a recent review [22], and references therein.

In bathy phytochromes, it has been found that in the photoactive (Pr) state of the chromophore in *Agp2*, proton migrations can take place. Although it has been suggested using pH-dependent changes that proton-transfer reactions occur between the chromophore and the protein[23], this reaction can take place intrachromophore[24]. Velazquez *et al.* propose that a proton transfer from the ring C nitrogen to carbonyl oxygen in ring D can occur, giving place to a keto-enol equilibrium, with the prevalence of the enol form at high pH[24].

<Figure 3>

Given the experimental evidence of enol form in the photoproduct, we explore the potential energy surface (PES) for the keto-enol tautomerism of the Pfr state of biliverdin (BV). In the present theoretical study, the focus is centered on the possible keto-enol tautomerization in both rings A and D of BV in the Pfr state. For BV, a model structure was considered without the external propionic groups, see Fig. 1(c). By inspection of Fig. 3, the keto-enol tautomerism could take place in either/both pyrrole ring A or/and pyrrole ring D to convert the lactam ring into a lactim. If we consider that a collection of keto-enol isomerization reactions could take place thermally in the photoinduced Pfr state, we can consider a set of tautomers as shown in Fig. 3. In Fig. 3, the different models of BV

in bacteriophytochrome are shown: di-lactam (DITAM), lactim on ring A (TIM-A), lactim on ring D (TIM-D) and finally di-lactim (DITIM).

In this study, we use quantum mechanical models to look for the possible formation of keto-enol tautomerisms in the signaling Pfr state. With that in mind, we look for the structural basis that could help to explain the bathochromic shift suffered by phytochrome upon interconversion from the Pr to the Pfr form.

MATERIALS AND METHODS

Computational Details. The lactam-lactim isomerization of the model system of BV was studied using density functional theory (DFT). Optimization of minima and transition states were carried out using the well-tested M06-2X functional[25–27] together with the *aug*-cc-pVDZ basis set[28]. The nature of all minima and transition states were confirmed through frequency calculations. All transition states were connected with the respective reactants and products through the intrinsic reaction coordinate (IRC) methodology[29–31]. To get reliable gas-phase energies, single-point calculations at the DLPNO-CCSD(T)/cc-pVTZ[28,32–35] on the gas phase geometries obtained at the M06-2X/*aug*-cc-pVDZ level of theory were performed. On the other hand, Gibbs free energies were computed using the quasi-rotor harmonic oscillator to treat low-frequency modes as reported by Grimme[36]. The aqueous and protein environments were accounted for using the polarizable continuum model (PCM)[37], with a dielectric constant of $\varepsilon = 4.0$[38–41]. For discussion purposes, energies in simulated protein environments were taken into account.

Rendering of structures and isosurfaces were done in *Chemcraft*[42], *CylView*[43] , and *PyMol*[44]. To reveal noncovalent interactions (NCIs), the NCIplot program of Johnson and co-workers was used[45,46]. However, for a quantitative rationale of NCIs of relevant structures, symmetry-adapted perturbation theory (SAPT)[47] was employed. Quantification of charge transfer effects was computed using the SAPT-CT approach[48–51]. All SAPT computations were performed at the SAPT0/cc-pVDZ level of theory in Psi4[52]. Specifically, DF–SAPT0[53–55] employing the cc-pVDZ-*ri* basis set was used for speeding up the computations. The SAPT interaction energy (ΔE_{int}) is composed as:

$$\Delta E_{int} = \Delta E_{elst} + \Delta E_{CT} + \Delta E_{disp} + \Delta E_{exch} + \Delta E_{pol} + \Delta E_{ind.} \quad (1)$$

The terms ΔE_{elst}, ΔE_{CT}, ΔE_{disp}, ΔE_{exch}, ΔE_{pol}, and ΔE_{ind} correspond to electrostatic, charge-transfer, dispersion, exchange, polarization, and induction energies. It should be noted that the polarization term is estimated from the induction and charge transfer term through $\Delta E_{ind} = \Delta E_{pol} + \Delta E_{CT}$.

We carried out an analysis based on the activation-strain model[56], also known as the distortion/interaction model, but using the precise SAPT methodology for obtaining the interaction energies, and the reliable coupled-cluster energies computed with DLPNO-CCSD(T) for activation

energies. Therefore, the activation energies ($\Delta E^{\ddagger}$) can be understood as composed by an interaction term ($\Delta E^{\ddagger}_{int}$) between the fragments, and a distortion term ($\Delta E^{\ddagger}_{dist}$) as follows:

$$\Delta E^{\ddagger} = \Delta E^{\ddagger}_{int} + \Delta E^{\ddagger}_{dist} \quad (2)$$

Time-dependent density functional theory (TD-DFT) calculations were performed on the stationary points on the potential energy surface (DITAM, TIM-A, TIM-D, and DITAM) to study the potential bathochromic shift of these different species. The B3LYP and CAM-B3LYP exchange-correlation functional was used together with the 6-31+G(d) Pople basis set[57,58]. On one hand, we performed geometry optimizations with the PCM module using ε = 4.0 to model the protein environment. Absorption spectra were obtained by computing 15 singlet excited states. On the other hand, the bilin chromophore has been extracted from the crystal structure of *Deinococcus radiodurans* phytochrome in the near-complete far-red light-absorbing Pfr state reported by Vierstra and coworkers (PDB: 5C5K)[16]. Having the tetrapyrrole backbone hydrogens were added and relaxed in the geometry optimization but leaving the backbone frozen. For the enolic forms, oxygen was also relaxed during geometry optimization. This approach, often called static approach, has been successfully applied in the study of phytochromes, which provides a snapshot of the conformational space of the protein[38,59,62]

RESULTS AND DISCUSSIONS

Paths Keto-Enol Tautomerization of the Bilin Chromophore: Non-Catalyzed and Water-Assisted Reaction Paths

In this section, the potential energy surface for the isomerization from DITAM to DITIM is studied. The isomerization of DITAM takes place under two consecutive proton transfer reactions from the N–H bond to the carbonyl moiety in pyrrole rings A and D (see Fig. 3). Transition state structures are collected in Fig. 4 with selected geometrical parameters. Transition state structures are characterized by a four-membered ring with the proton migrating from the nitrogen to the oxygen atom (see Fig. 4). At the TS structure, there is a noticeable contraction of the NCO angle to allow a feasible proton migration. On average the contraction of the NCO angle is quite similar in both rings with 14.4 and 15.7 degrees, at ring A and ring D, respectively.

Energetics for the enolization reaction of DITIM was obtained and shown in Fig. 3. For gas-phase energies, high-level coupled-cluster energies were computed. Activation energies $\Delta E_i^{\ddagger}$ $(i = 1 - 4)$ are reported in Table I together with Gibbs free energies in protein environments (see Computational Procedure section for details). The respective energy profile for the successive keto-enol tautomerization simulating the chromophore pocket is reported in Fig. 5(a).

First, DITAM can undergo two different keto-enol tautomerizations: in ring A or in ring D to form either TIM-A or TIM-D, respectively (Fig. 3). Activation energies in the gas phase for the formation of TIM-A and TIM-D were found to be $\Delta E_1^{\ddagger}$ = 45.9 and $\Delta E_2^{\ddagger}$ = 53.7 kcal mol^{-1}, respectively. Moreover, reaction energies for the formation of TIM-A and TIM-D amount to 2.0 and 12.1 kcal mol^{-1}, respectively. Therefore, the proton transfer in ring A is both kinetically and thermodynamically favored when comparing with ring D, but difficult to take place in normal protein conditions due to the height of the energy barrier. On the other hand, TIM-A and TIM-D can undergo a second proton transfer in ring D and ring A, with activation energies of $\Delta E_4^{\ddagger}$ = 45.0 and $\Delta E_3^{\ddagger}$ = 52.5 kcal mol^{-1}, respectively (gas phase).

Gibbs free energy changes for the isomerization mechanism of DITAM were also studied in the protein environment, simulated through the PCM formalism. For comparison, energies were also computed in water (see Supporting Information). Although there is a clear difference in the dielectric constant of water (ε = 78.35*D*) and the protein (ε = 4.00*D*), it does not have a tremendous effect on the obtained Gibbs free energies as previously reported by Matute et al.[38]. On average, the differences in Gibbs free energies in water and protein environments are near to just 1 kcal mol^{-1}.

<Figure 4>

<Table 1>

It is clear from Table 1 a noticeable decrease in the activation energy in protein environments when compared with the gas phase energies. The energy profile for the isomerization pathway is shown in Fig. 5(a). The activation energy for the proton transfer reactions in ring A and ring D of DITAM were found to be 38.9 and 45.7 kcal mol^{-1}, also evidencing an exothermic formation of TIM-A (2.2 kcal mol^{-1}) and TIM-D (11.3 kcal mol^{-1}). On the other hand, $\Delta G_3^{\ddagger}$ and $\Delta G_4^{\ddagger}$ energies are 40.5 and 47.1 kcal mol^{-1}. From the results, it can be concluded that the lactam-lactim isomerization in ring A

and ring D in DITAM is highly unfavored to take place in ambient reaction conditions. The lowered thermodynamic stability of both TIM-A and TIM-D compared to DITAM makes the process even more unlikely to take place. It is worth mentioning that the formation of TIM-D is kinetically and thermodynamically less favored that formation of TIM-A. The gain in thermodynamic stability of TIM-A may be triggered by the formation of the enol product, promoting a lowering of the strain energy caused by the three pyrrole N–H bonds in rings A, B, and C. It is observed since, in DITAM, the three hydrogens are pointing out of the plane while in TIM-A they are almost aligned with the respective pyrrole ring. In contrast, in the formation of TIM-D, the N–H bonds in rings A, B, and C are unaltered. A second proton-transfer reaction in TIM-A or TIM-D can produce a full enolic structure (DITIM), which was found to be even more unlikely to take place regarding larger activation energies than a first isomerization reaction and lowered thermodynamic stabilization. In summary, in the absence of water molecules, possible keto-enol tautomerism is thought not to be possible with the equilibrium highly displaced to the formation of the keto form. With these results, we confirm that intra-pyrrole keto-enol equilibrium is not possible in protein conditions, albeit IR studies have suggested the preponderance of the enolic form at high pH but through deprotonation of ring C[24]. To study the feasibility of the keto-enol tautomerization in normal protein conditions, we consider the presence of water molecules.

It is well known that water molecules can access the chromophore pocket of phytochromes (see Fig. 1(b) and Fig. 7(a)). Feliks *et al.* studied the mobility of water molecules in the chromophore binding domain of the *Deinococcus radiodurans* bacteriophytochrome by molecular dynamic simulations[60] (PCB: 2O9C). The authors found that water molecules in the chromophore pocket can be exchanged by water molecules from the solvent. Interestingly, it was found that the region comprehended among the pyrrole rings was always occupied by at least one water molecule, which is connected to the outer solvent molecules employing a network of multiple hydrogen bonds[60] (see Fig. 7(a) for reference). In Fig. 7(a) we show the crystal structure of a bilin chromophore found in *Deinococcus radiodurans* in the Pfr form[16]. The crystal structure reveals a water molecule stabilized through hydrogen bonds at the center of ring A, B, and C. Further inspection of nearby residues of ring D we noticed that the –COOH and –OH groups of D207 and S468 are pointing in the direction of the N–H bond at ring D. This finding could explain a possible stabilizing interaction of the residues with a water molecule to carry out an assisted keto-enol tautomerism. This evidence prompted us to study the possibility of a water-catalyzed keto-enol tautomerization to get a possible structural

interpretation of the bathochromic shift of the Q-band in the Pr to Pfr conversion. To study the possibility of a catalyzed keto-enol equilibrium, the water-assisted isomerization was considered using an explicit water molecule in the computations. The respective reaction profile is shown in Fig. 5(b). Activation Gibbs free energies can be found at the bottom part of Table 1. Transition state structures for the water-catalyzed reactions are shown in Fig. 6.

<Figure 5>

Particularly, water-assisted reactions are characterized by 6-membered transition state structures, in contrast with the more strained 4-membered TS in the non-catalyzed reaction path. This difference in the strain energy to reach the respective transition state is one of the fundamental reasons for the decrease in energy barriers. In presence of one water molecule activation free energies decrease up to ~30 kcal mol^{-1} (for $\Delta G_4^{\ddagger}$). The formation of a reactant complex between DITAM and H_2O gives rise to either DITAM(A) or DITAM(D), with the equilibrium displaced to the formation of DITAM(A) with a ΔG° = −1.5 kcal mol^{-1} over DITAM(D), ΔG° = 3.6 kcal mol^{-1}. It is worth noting, that the energies reported above may be lowered by the interaction of the surrounding amino acids. Activations free energy for the first catalyzed keto-enol tautomerization was found to be 12.9 and 20.3 kcal mol^{-1} at pyrrole ring A and D, respectively. From the results, we can see that the competing keto-enol tautomerization can easily take place in ring A to form TIM-A over ring D because of a higher energy barrier. This is a quite remarkable result since due to the low energy barrier for the formation of TIM-A, its formation cannot be discarded. The second energy barrier for the transformation of the species into the full enolic form, DITIM, is 13.1 and 17.3 through ***w*TS3** and ***w*TS4**, respectively. It is worth noting from the energy profile that the keto-enol equilibrium is thought to be more displaced to the keto form, but regarding the low energy barrier towards TIM-A, the formation of the enol product is highly feasible.

<Figure 6>

<Figure 7>

To analyze the nature of the energy barrier in terms of distortion energy of the reactants (BV isomer and H_2O) and the interaction energy to reach the TS structure, we employed a distortion-interaction based model using the well-defined SAPT energies (see Computational Details section for details). The activation ($\Delta E^{\ddagger}$) distortion ($\Delta E^{\ddagger}_{dist}$) and interaction ($\Delta E^{\ddagger}_{int}$) energies are plotted in Fig. 6. It was observed that for the water-catalyzed proton transfer reactions in ring A, they present a more pronounced stabilizing interaction component (−70.5 and −67.2 kcal mol^{-1} for ***w*TS1** and ***w*TS3**), being it less stabilizing for the proton transfer in ring D (−54.2 and −52.2 kcal mol_{-1} for ***w*TS2** and ***w*TS4**). However, when the keto-enol tautomerization takes place in ring D, the lowering of the activation energies is due to lower distortion energy when compared to ring A. Further explorations of the distortion energy component gave us some interesting insights into the source (chromophore or water) of this term. We found for the keto-enol tautomerism in ring A, the water molecule is responsible for near 69% of $\Delta E^{\ddagger}_{dist}$ while only 31% is due to distortions in the BV chromophore. On the other hand, when the catalyzed proton transfer reaction occurs in ring D, the source of the distortion component is inverted, with 77% of the distortion coming from the chromophore and just 23% from the water molecule. Inspection of the reaction paths up to the respective TSs revealed that the greater distortion component coming from the water molecule (in-ring A) is due to the movement of the water from out of the plane (considering the pyrrole units) towards it, to carry out the catalysis. The water molecule is highly stabilized out-of-plane through hydrogen bonds (HBs). On the contrary, when the reactions take place in ring D, in the absence of HBs, the water molecule is already on the plane to carry out the assisted proton-transfer reaction. Therefore, we think that the movement and distortion of H_2O trigger the movement of the network of water molecules in the chromophore pocket imposing possible conformational changes in the protein.

It is worth noting that although lower activation energies are obtained compared to the non-catalyzed path, the formation of enol derivatives is still non-spontaneous, but likely to take place in ring A, and probably easy at high pH[24]. Therefore, we conclude that the reaction would take place under kinetic control. Moreover, the main reason for the increased stabilization of the keto forms is due to the formation of stronger HBs.

Regarding barrier heights of the proper keto-enol tautomerizations, the process is very hard to take place, albeit most likely to take place assisted by a water molecule. However, tunneling

governed proton transfer reactions can easily take place as reported by P. Löwdin in the 60s to explain mutations in DNA[63]. To reveal the possible action of tunneling effects on the keto-enol tautomerization in BV, the tunneling crossover temperature (T_x) introduced by Fermann and Auerbach[64] was employed (see Supporting Information for further details and discussion). Interpretation of the T_x index is straightforward: temperatures below T_x indicates the boundary in which tunneling effects operate. Interestingly, the T_x for both non-catalyzed and catalyzed reactions is above 400K, which indicates that tunneling effect may govern the formation of the enolic derivatives.

Albeit less-strained TS structures decrease considerably the energy barrier for the tautomerism, we found that when the proton transfer reaction takes place in ring A (***w*TS1** and ***w*TS3**), enhanced stabilization is gained through multiple HBs. However, due to the chemical environment at the vicinity of ring D, no further stabilization is gained at the TS through the formation of HBs with the pyrrole hydrogens with water. This last finding is supported by an inspection of the non-covalent interaction (NCI) index shown in Fig. 7. ***w*TS1** and ***w*TS2** pathways are shown in Fig. 7 for comparing purposes, and because these are the two more likely paths to take place. The NCI index reveals three HBs with different strengths for DITAM(A) (blue-ish isosurfaces) and two HBs for DITAM(D). Furthermore, attractive London dispersion forces can be also observed, characterized predominantly by CH···CH-type interactions along with the structures (greenish isosurfaces, see Supporting Information for full NCI images). From Fig. 7(b), the NCI isosurfaces reveal that the further stabilization at the TS structure is due to an HB formed by the N–H bond in ring C and the O–H moiety in the water molecule, with an OH···HN(ring C) distance of 1.799 Å.

To quantitatively reveal noncovalent interactions in the two most possible keto-enol tautomerizations, symmetry-adapted perturbation theory (SAPT) components were computed along the reaction coordinate to reveal the change of the different energy components for the water-assisted keto-enol tautomerism taking place in ring A and D (see Fig. 8). The DITIM(A) species is higher stabilized (−15.0 kcal mol^{-1} with a SAPT interaction energy of −24.6 kcal mol^{-1}) than DITIM(D) (3.6 kcal mol^{-1} with a SAPT interaction energy of −12.8 kcal mol^{-1}) due to the extra stabilization through the formation of three strong HBs over two HBs in the latter structure. From the SAPT results, it was found that the electrostatic component predominates (followed by the induction and dispersion components) in the interaction between DITAM and H_2O, −29.6 kcal mol^{-1} and −15.9 kcal mol^{-1} for the isomerization in ring A and ring D, respectively. Interestingly, charge transfer,

dispersion, and polarization components are quite steady at the onset of the reaction. However, all energy components become more stabilizing as reaching the TS structure.

In summary, from the energetic results and taking into account the evidence from the different analyses we can conclude that a possible keto-enol tautomerization can take place mainly involving the formation of TIM-A. This is supported by a low activation energy of 12.9 kcal mol^{-1}, and with pronounced stabilization of the enol form through HBs. Furthermore, since a water molecule is always present in the crystal structure (see Fig. 7 (a)) of the chromophore, our computations suggest that the prominent formation of TIM-A, over all other tautomers, cannot be ignored. Finally, the results suggest that after the *15Z* to *15E* photoisomerization reaction of BV takes place possible water-catalyzed keto-enol tautomerizations can take place with the prominent formation of the TIM-A isomer (over all other isomers) should be considered as a potential form in the Pfr state of BV.

<Figure 8>

Absorption Spectra of Keto/Enol Tautomers

To study the photophysical properties of the different tautomers of the BV chromophore, TD-DFT computations were performed. The absorption spectra of phytochromes are recognized by showing two intense bands. A low-energy band namely Q-band is more intense than a second high-energy band called Soret band (B-band). The Q-band has an absorption peak in the visible region (660-700 nm) while the Soret band is found in the near-UV region (380-420 nm) of the electromagnetic spectrum in the Pr form[61]. A recent study has shown the crystallographic structure of bacteriophytopchrome in the Pfr state[16]. The authors found the λ_{max} for the Q-band at 754 nm. To simulate the absorption spectra, we have used a static model based on the crystal structure of bilin (see Computational Details Section), and by optimizing the geometry of all tautomers to the minimum energy conformation. The simulated absorption spectra using the static model is shown in Fig. 9. Excited states, wavelength, oscillator strengths, and description of the bands for the two main bands are found in Table 2.

The Q-band arises predominantly from an allowed HOMO to LUMO electronic transition to yield the S_1 state in most cases. From inspection of the HOMO and LUMO isosurfaces shown in Fig. 10, it can be noticed that this band is predominantly composed of $\pi \rightarrow \pi^*$ transitions with $n \rightarrow \pi^*$ and $n \rightarrow n^*$ also contributing but in a minor extent. Although experimentally the Q- band shows a shoulder it is not exposed in the simulated spectrum most likely due to the lack of vibronic coupling in the computation of excitations.

<Figure 9>

<Table 2>

According to the TD-DFT calculations on the BV in the Pfr form of the canonical phytochrome, the keto-enol tautomerism slightly affects the shift of the Q-band when the vertical excitation was calculated from optimized geometries. Moreover, when the optimized geometries are used, the λ_{max} is not in good agreement with one reported experimentally for DITAM but remains close to the one computed using the crystal structure. Nonetheless, the results were different when the calculations were performed directly on the crystallographic geometry, assuming that such a structure should be a reasonably good snapshot along the conformational space of the protein. In this case, the DITAM gives a vertical excitation of ca. 730 nm, which is in excellent agreement with the experimental value. On the other hand, TIM-A and DITIM were red-shifted in around 15 nm when compared with DITAM. Noteworthy, this approach was also successfully implemented in our previous studies on the bilin chromophore for both cyanobacterial phytochrome Cph1 and plant phytochrome, with excellent agreement between the calculated and experimental absorption spectra[38,59]. A similar static model to calculate these UV-Vis spectra for BV in bacteriophytochrome was recently reported by Mennucci and co-workers[62], who also compared the static model with a dynamic model (i.e., with snapshots taken from molecular dynamics simulations), although they concluded that the dynamic model does not significantly affect the absorption spectra since the chromophore seems to be very stable in its binding pocket and no major fluctuations were detected for the H-bond network between the bilin, the surrounding residues, and the water molecules. This is the main reason why the analysis is based on the absorption spectra form the crystallographic structures. Absorption spectra were also computed using the long-range corrected CAM-B3LYP using the same basis set. The λ_{max} for DITAM, 666 nm, was found to be blue-shifted with respect to the one obtained with the B3LYP functional, and off from the experimental value by 88 nm. However,

it is capable to reproduce the red-shift of the enolic tautomers: 751, 725, and 755 nm for TIM-A, TIM-D, and DITIM.

Experimentally, the Q-band suffers a red-shift in the transition from the Pr to the Pfr state. Based on the results of the previous section, we found that it is highly possible that water-catalyzed keto-enol tautomerization can take place in ring A with low activation energy (12.9 kcal mol^{-1}) being able to yield a keto-enol equilibrium. Interestingly, it was found from the TD-DFT results that TIM-A produces a considerable bathochromic shift (ca 15 nm), which can contribute to the experimentally observed shift of the Q-band in the Pfr form. Although TIM-D produces an ipsochromic shift, its formation together with the DITIM conformer is thought to be less probable. Even though, the CAM-B3LYP results show a red-shift for all the enolic tautomers, that would reinforce the idea of the formation of keto-enol tautomerisms in the Pfr form of BV. Moreover, we tested the effect on the Q-band when the explicit (crystallopgraphic) water molecule is included in the computations. Both B3LYP and CAM-B3LYP functionals showed the practically the same λ_{max} whether the water molecule is included or not in the computations. Although the water molecule is interacting with the chromophore, the HOMO and LUMO are delocalized only over the pyrrolic structure.

Our analysis and results suggest that after the Pr→Pfr isomerization, possible water-catalyzed proton transfer reactions can take place in ring A that could help in the redshift of the Q-band in bacteriophytochromes. Overall, our results suggest that the keto-enol tautomerism of biliverdin in bacteriophytochrome is energetically viable and with UV-Visible absorption bands in reasonable agreement with the experimental data. This keto-enol equilibrium is likely favoring the lactam tautomer, although such equilibrium could eventually be shifted in favor of the lactim tautomer (TIM-A). It is worth to mention that the lactim tautomer has been reported to appear in the dark reversion mechanism of bathy phytochromes. Hence, the present work should be certainly useful to advance the mechanistic understanding of phytochromes in nonoxygenic bacteria.

<Figure 10>

CONCLUSIONS

Based on the experimental evidence of the presence of water molecules in the chromophore pocket of phytochromes, the possibility of keto-enol tautomerisms was studied in biliverdin. This study is supported by the evidence of the presence of keto-enol equilibrium through deprotonation of the N–H group in ring C. Particularly, we studied the intramolecular occurrence of keto-enol tautomerism through the adjacent pyrrole N–H group to the carbonyl moiety in both ring A and ring D, without deprotonation of the tetrapyrrole backbone. The results suggest that this isomerization is not possible in the absence of a water molecule due to high activation energies toward the formation of the enol tautomer. However, the water catalyzed process is very likely to take place in ring A with an activation Gibbs free energy of ~12.9 kcal mol^{-1}. The drastic lowering in the activation energy for the keto-enol tautomerism is due to the stabilization of the water moiety through hydrogen bonds along the reaction coordinate.

Our results suggest that the keto-enol tautomerism of biliverdin in bacteriophytochrome is energetically viable to take place. This evidence is supported by UV-Visible absorption bands in reasonable agreement with the experimental data. Although the keto-enol equilibrium is likely favoring the lactam tautomer, the equilibrium could eventually be shifted in favor of the TIM-A as it has been reported to occur in the dark reversion mechanism of bathy phytochromes. We believe that the present work will be useful to advance in the mechanistic understanding of phytochromes in nonoxygenic bacteria.

ACKNOWLEDGEMENTS

The authors acknowledge financial support from FONDECYT Grant No. 1181260.

SUPPORTING INFORMATION

Additional supporting information may be found online in the Supporting Information section at the end of the article:

Figure S1. Energy profile in water and protein environments for the non-catalyzed keto-enol tautomerization.

Figure S2. Noncovanlent interaction (NCI) index for ***w*TS1** and ***w*TS2** reaction path. Letters A and D within parenthesis indicate the position of the water molecule in ring-A and ring-D, respectively.

Table S1. Zero-point corrected activation energies ($DU^{\ddagger}_{0}$), vibrational frequency of the reactive mode ($v^{\ddagger}$), and tunneling crossover temperatures (T_x) for the non-catalyzed and water catalyzed keto enol reactions.

Figure S3. SAPT profile together with NCI isosurfaces for ***w*TS1** and ***w*TS2** reaction paths.

Figure S4. Energy gap together with densities of the HOMO and LUMO orbitals. Energiess are given in eV.

Figure S5. Absorption spectra for the optimized structures at the B3LYP/6-31+G(d) level of theory

Table S2. Absorption maximum lmax, oscillator strength, and monoexcitations for the Q-band for for DITAM and w-DITAM from the crystal extructure stracted from PDB: 6SAW (Idiomarina species A28L (IsPadC))

Figure S6. HOMO and LUMO isosurfaces for DITAM and w-DITAM from the crystal extructure stracted from PDB: 6SAW (Idiomarina species A28L (IsPadC))

REFERENCES

[1]S.-H. Wu and J. Lagarias (1997) The phytochrome photoreceptor in the green alga Mesotaenium caldariorum: Implication for a conserved mechanism of phytochrome action. *Plant Cell Environ.* **20**, 691–699.

[2]S.-H. Wu, M. T. McDowell, and J. C. Lagarias (1997) Phycocyanobilin is the natural precursor of the phytochrome chromophore in the green alga Mesotaenium caldariorum. *J. Biol. Chem.* **272**, 25700–25705.

[3]A. Blumenstein, K. Vienken, R. Tasler, J. Purschwitz, D. Veith, N. Frankenberg-Dinkel, and R. Fischer (2005) The Aspergillus nidulans phytochrome FphA represses sexual development in red light. *Curr. Biol.* **15**, 1833–1838.

[4]A. C. Froehlich, B. Noh, R. D. Vierstra, J. Loros, and J. C. Dunlap (2005) Genetic and molecular analysis of phytochromes from the filamentous fungus Neurospora crassa. *Eukaryot. Cell* **4**, 2140–2152.

[5]B. Karniol, J. R. Wagner, J. M. Walker, and R. D. Vierstra (2005) Phylogenetic analysis of the phytochrome superfamily reveals distinct microbial subfamilies of photoreceptors. *Biochem. J.* **392**, 103–116.

[6]W. R. Briggs and J. L. Spudich, Handbook of Photosensory Receptors (John Wiley & Sons, 2005).

[7]N. C. Rockwell, Y.-S. Su, and J. C. Lagarias (2006) Phytochrome structure and signaling mechanisms. *Annu. Rev. Plant Biol.* **57**, 837–858.

[8]S. Brandt, D. von Stetten, M. Günther, P. Hildebrandt, and N. Frankenberg-Dinkel (2008) The fungal phytochrome FphA from Aspergillus nidulans. *J. Biol. Chem.* **283**, 34605–34614.

[9]V. De Riso, R. Raniello, F. Maumus, A. Rogato, C. Bowler, and A. Falciatore (2009) Gene silencing in the marine diatom Phaeodactylum tricornutum. *Nucleic Acids Res.* **37**, e96–e96.

[10]N. C. Rockwell and J. C. Lagarias (2010) A brief history of phytochromes. *ChemPhysChem* **11**, 1172–1180.

[11]N. Lenngren, P. Edlund, H. Takala, B. Stucki-Buchli, J. Rumfeldt, I. Peshev, H. Häkkänen, S. Westenhoff, and J. A. Ihalainen (2018) Coordination of the biliverdin D-ring in bacteriophytochromes. *Phys. Chem. Chem. Phys.* **20**, 18216–18225.

[12]S.-H. Wu and J. C. Lagarias (2000) Defining the bilin lyase domain: lessons from the extended phytochrome superfamily. *Biochemistry* **39**, 13487–13495.

[13]T. Lamparter, N. Michael, O. Caspani, T. Miyata, K. Shirai, and K. Inomata (2003) Biliverdin binds covalently to Agrobacterium phytochrome Agp1 via its ring a vinyl side chain. *J. Biol. Chem.* **278**, 33786–33792.

[14]T. Lamparter, M. Carrascal, N. Michael, E. Martinez, G. Rottwinkel, and J. Abian (2004) The biliverdin chromophore binds covalently to a conserved cysteine residue in the N-terminus of Agrobacterium phytochrome Agp1. *Biochemistry* **43**, 3659–3669.

[15]B. Quest and W. Gärtner (2004) Chromophore selectivity in bacterial phytochromes: dissecting the process of chromophore attachment. *Eur. J. Biochem.* **271**, 1117–1126.

[16]E. S. Burgie, J. Zhang, and R. D. Vierstra (2016) Crystal structure of Deinococcus phytochrome in the photoactivated state reveals a cascade of structural rearrangements during photoconversion. *Structure* **24**, 448–457.

[17]B. Karniol and R. D. Vierstra (2003) The pair of bacteriophytochromes from Agrobacterium tumefaciens are histidine kinases with opposing photobiological properties. *Proc. Nat. Acad. Sci. USA* **100**, 2807–2812.

[18]M. G. Müller, I. Lindner, I. Martin, W. Gärtner, and A. R. Holzwarth (2008) Femtosecond kinetics of photoconversion of the higher plant photoreceptor phytochrome carrying native and modified chromophores. *Biophys. J.* **94**, 4370–4382.

[19]C. Slavov, X. Xu, K.-h. Zhao, W. Gärtner, and J. Wachtveitl (2015) Detailed insight into the ultrafast photoconversion of the cyanobacteriochrome Slr1393 from Synechocystis sp. *Biochim. Biophys. Acta* **1847**, 1335–1344.

[20]P. W. Kim, L. H. Freer, N. C. Rockwell, S. S. Martin, J. C. Lagarias, and D. S. Larsen (2012) Femtosecond photodynamics of the red/green cyanobacteriochrome NpR6012g4 from Nostoc punctiforme. 1. Forward dynamics. *Biochemistry* **51**, 608–618.

[21]P. W. Kim, L. H. Freer, N. C. Rockwell, S. S. Martin, J. C. Lagarias, and D. S. Larsen (2012) Femtosecond photodynamics of the red/green cyanobacteriochrome NpR6012g4 from Nostoc punctiforme. 2. Reverse dynamics. *Biochemistry* **51**, 619–630.

[22]V. Sineshchekov and O. Bekasova (2019) Two distinct photoprocesses in cyanobacterial bilin pigments: Energy migration in light-harvesting phycobiliproteins versus photoisomerization in phytochromes. *Photochem. Photobiol*. (in press). DOI: 10.1111/php.13197

[23]B. Zienicke, I. Molina, R. Glenz, P. Singer, D. Ehmer, F. V. Escobar, P. Hildebrandt, R. Diller, and T. Lamparter (2013) Unusual spectral properties of bacteriophytochrome Agp2 result from a deprotonation of the chromophore in the red-absorbing form Pr. *J. Biol. Chem.* **288**, 31738–31751.

[24]F. V. Escobar, P. Piwowarski, J. Salewski, N. Michael, M. F. Lopez, A. Rupp, B. M. Qureshi, P. Scheerer, F. Bartl, N. Frankenberg-Dinkel, et al. (2015) A protonation-coupled feedback mechanism controls the signalling process in bathy phy- tochromes. *Nat. Chem.* **7**, 423.

[25]Y. Zhao and D. G. Truhlar (2008) The m06 suite of density functionals for main group thermochemistry, thermochemical kinetics, noncovalent interactions, excited states, and transition elements: Two new functionals and systematic testing of four m06-class functionals and 12 other functionals. *Theor. Chem. Acc.* **120**, 215–241.

[26]Y. Zhao and D. G. Truhlar (2008) Exploring the limit of accuracy of the global hybrid meta density functional for main-group thermochemistry, kinetics, and noncovalent interactions. *J. Chem. Theory Comput.* **4**, 1849–1868.

[27]R. Valero, R. Costa, I. de PR Moreira, D. G. Truhlar, and F. Illas (2008) Performance of the m06 family of exchange-correlation functionals for predicting magnetic coupling in organic and inorganic molecules. *J. Chem. Phys.* **128**, 114103.

[28]T. H. Dunning (1989) Gaussian basis sets for use in correlated molecular calculations. I. The atoms boron through neon and hydrogen. *J. Chem. Phys.* **90**, 1007–1023.

[29]K. Fukui (1981) The path of chemical reactions-the IRC approach. *Acc. Chem. Res.* **14**, 363–368 (1981).

[30]H. P. Hratchian and H. B. Schlegel (2004) Accurate reaction paths using a hessian based predictor-corrector integrator. *J. Chem. Phys.* **120**, 9918–9924.

[31]H. P. Hratchian and H. B. Schlegel (2005) Using hessian updating to increase the efficiency of a hessian based predictor-corrector reaction path following method. *J. Chem. Theory Comput.* **1**, 61–69.

[32]C. Riplinger and F. Neese (2013) An efficient and near linear scaling pair natural orbital based local coupled cluster method. *J. Chem. Phys.* **138**, 034106.

[33]C. Riplinger, B. Sandhoefer, A. Hansen, and F. Neese (2013) Natural triple excitations in local coupled cluster calculations with pair natural orbitals. *J. Chem. Phys.* **139**, 134101.

[34]D. G. Liakos, M. Sparta, M. K. Kesharwani, J. M. Martin, and F. Neese (2015) Exploring the accuracy limits of local pair natural orbital coupled-cluster theory. *J. Chem. Theory Comput.* **11**, 1525–1539.

[35]D. G. Liakos and F. Neese (2015) Is it possible to obtain coupled cluster quality energies at near density functional theory cost? domain-based local pair natural orbital coupled cluster vs mod- ern density functional theory. *J. Chem. Theory Comput.* **11**, 4054–4063.

[36]S. Grimme (2012) Supramolecular binding thermodynamics by dispersion-corrected density functional theory. *Chem. Eur. J.* **18**, 9955–9964.

[37]J. Tomasi, B. Mennucci, and R. Cammi (2005) Quantum mechanical continuum solvation models. *Chem. Rev.* **105**, 2999–3094 (2005).

[38] R. A. Matute, R. Contreras, G. Pérez-Hernández, and L. González (2008) The chromophore structure of the cyanobacterial phytochrome Cph1 as predicted by time-dependent density functional theory. *J. Phys. Chem. B* **112**, 16253–16256.

[39]M. R. Blomberg, P. E. Siegbahn, and G. T. Babcock (1998) Modeling electron transfer in biochemistry: A quantum chemical study of charge separation in Rhodobacter s phaeroides and photosystem II. *J. Am. Chem. Soc.* **120**, 8812–8824.

[40]J. Wan, X. Xu, Y. Ren, and G. Yang (2005) A time dependent density functional theory study of α-84 phycocyanobilin chromophore in c-phycocyanin. *J. Phys. Chem. B* **109**, 11088–11090.

[41]Y. Ren, J. Wan, X. Xu, Q. Zhang, and G. Yang (2006) A time-dependent density functional theory investigation of the spectro- scopic properties of the β-subunit in c-phycocyanin. *J. Phys. Chem. B* **110**, 18665–18669.

[42]G. Zhurko and D. Zhurko, “Chemcraft, version 1.6,” URL: http://www. chemcraftprog. com (2009).

[43]C. Legault, “Cylview, 1.0 b,” Universit´e de Sherbrooke (2009).

[44] The PyMOL Molecular Graphics System, Version 2.0 Schrödinger, LLC.

[45]E. R. Johnson, S. Keinan, P. Mori-Sanchez, J. Contreras-Garcia, A. J. Cohen, and W. Yang (2010) Revealing noncovalent interactions. *J. Am. Chem. Soc.* **132**, 6498–6506.

[46]J. Contreras-García, E. R. Johnson, S. Keinan, R. Chaudret, J.- P. Piquemal, D. N. Beratan, and W. Yang (2011) NCIPLOT: A program for plotting noncovalent interaction regions. *J. Chem. Theory Comput.* **7**, 625–632.

[47]B. Jeziorski, R. Moszynski, and K. Szalewicz (1994) Perturbation theory approach to intermolecular potential energy surfaces of van der waals complexes. *Chem. Rev.* **94**, 1887–1930.

[48]A. J. Stone (1993) Computation of charge-transfer energies by perturbation theory. *Chem. Phys. Lett.* **211**, 101–109.

[49]R. Z. Khaliullin, E. A. Cobar, R. C. Lochan, A. T. Bell, and M. Head-Gordon (2007) Unravelling the origin of intermolecular interactions using absolutely localized molecular orbitals. *J. Phys. Chem. A* **111**, 8753–8765.

[50]A. J. Stone and A. J. Misquitta (2009) Charge-transfer in symmetry-adapted perturbation theory. *Chem. Phys. Lett.* **473**, 201–205.

[51]A. J. Misquitta (2013) Charge transfer from regularized symmetry-adapted perturbation theory. *J. Chem. Theory Comput.* **9**, 5313–5326.

[52]R. M. Parrish, L. A. Burns, D. G. Smith, A. C. Simmonett, A. E. DePrince III, E. G. Hohenstein, U. Bozkaya, A. Y. Sokolov, R. Di Remigio, R. M. Richard, J. F. Gonthier, A. M. James, H. R. McAlexander, A. Kumar, M. Saitow, X. Wang, B. P. Pritchard, P. Verma, H. F. Schaefer III, K. Patkowski, R. A. King, E. F. Valeev, F. A. Evangelista, J. M. Turney, T. D. Crawford, and C. D. Sherrill (2017) Psi4 1.1: An open-source electronic structure program emphasizing automation, advanced libraries, and interoperability. *J. Chem. Theory Comput.* **13**, 3185–3197.

[53]E. G. Hohenstein and C. D. Sherrill (2010) Density fitting and cholesky decomposition approximations in symmetry-adapted perturbation theory: Implementation and application to probe the nature of π − π interactions in linear acenes. *J. Chem. Phys.* **132**, 184111.

[54]E. G. Hohenstein and C. D. Sherrill (2010) Density fitting of intramonomer correlation effects in symmetry-adapted perturbation theory. *J. Chem. Phys.* **133**, 014101.

[55]E. G. Hohenstein, R. M. Parrish, C. D. Sherrill, J. M. Turney, and H. F. Schaefer III (2011) Large-scale symmetry-adapted perturbation theory computations via density fitting and Laplace transformation techniques: Investigating the fundamental forces of DNA-intercalator interactions. *J. Chem. Phys.* **135**, 174107.

[56]F. M. Bickelhaupt and K. N. Houk (2017) Analyzing reaction rates with the distortion/interaction-activation strain model. *Angew. Chem. Int. Ed.* **56**, 10070–10086.

[57]J. D. Dill and J. A. Pople (1975) Self-consistent molecular orbital methods. XV. Extended gaussian-type basis sets for lithium, beryllium, and boron. *J. Chem. Phys.* **62**, 2921–2923.

[58]M. M. Francl, W. J. Pietro, W. J. Hehre, J. S. Binkley, M. S. Gor- don, D. J. Drefrees, and J. A. Pople (1982) Self-consistent molecular orbital methods. XXIII. A polarization-type basis set for second-row elements. *J. Chem. Phys.* **77**, 3654–3665.

[59]R. A. Matute, R. Contreras, and L. González (2010) Time-dependent DFT on phytochrome chromophores: A way to the right conformer. *J. Phys. Chem. Lett.***1**, 796–801.

[60]M. Feliks, C. Lafaye, X. Shu, A. Royant, and M. Field (2016) Structural determinants of improved fluorescence in a family of bacteriophytochrome-based infrared fluorescent proteins: Insights from continuum electrostatic calculations and molecular dynamics simulations. *Biochemistry* **55**, 4263–4274.

[61] I. V. Polyakov, B. L. Grigorenko, V. A. Mironov, and A. V. Nemukhin (2018) Modeling structure and excitation of biliverdin-binding domains in infrared fluorescent proteins. *Chem. Phys. Lett.* **710**, 59–63.

[62]V. Macaluso, L. Cupellini, G. Salvadori, F. Lipparini, and B. Mennucci (2020) Elucidating the role of structural fluctuations, and intermolecular and vibronic interactions in the spectroscopic response of a bacteriophytochrome. *Phys. Chem. Chem. Phys*.

[63]P. O. Löwdin (1963) Proton tunneling in DNA and its biological implications. *Reviews of Modern Physics*, **35**, 724.

[64] J. T. Fermann and S. Auerbach (2000) Modeling proton mobility in acidic zeolite clusters: II. Room temperature tunneling effects from semiclassical rate theory *J. Chem. Phys.* **112**, 6787–6794.

Figure Captions

Figure 1. (a) BV chromophore, (b) structure of BV in Pr form from the crystal structure of bacteriophytochrome[11], and (c) Photoisomerization of model BV between the *15Z* to *15E* conformers. Red spheres in (b) represent crystallographic water molecules.

Figure 2. Diagram for the photochemical cycle for prototypical phytochromes. Spatial orientation of the C15=C16 bond is shown in brackets.

Figure 3. Model structures under consideration for consecutive keto-enol tautomerizations of BV. Gas phase Gibbs free energies of activation are reported in in Table 1.

Figure 4. Transition state structures for all possible proton transfer reactions. Bond distances and angles are reported in Å and degrees, respectively.

Figure 5. Gibbs free energy profile for the isomerization of DITAM in protein environments (a) non-catalyzed reaction and (b) water catalyzed reaction. letter "A" and "D" within parenthesis indicate position of the water molecule, either in ring A or ring D, respectively.

Figure 6. Water-assisted transition state structures for the different isomers. Bar plot shows activation, distortion and interaction energies (in gas phase). All energies are reported in kcal mol−1. Bond distances and angles are reported in Å and degrees, respectively.

Figure 7. (a) Crystal structure of BV in the Pfr form of in *Deinococcus radiodurans* phytochrome[16] (b) Non-covalent interaction (NCI) index for the keto-enol tautomerism of DITAM in ring A, DITAM(A), and ring D, DITAM(D).

Figure 8. Symmetry-adapted perturbation theory (SAPT) computations for the keto-enol tautomerization of DITAM in ring A (solid line) and ring D (dotted line). Energy component are showed in color-code. Sub-indices abbreviations *elst*, *CT, disp, exch, pol, int,* and *ind* stand for electrostatics, charge-transfer, dispersion, exchange, polarization, interaction (or SAPT energy), and induction.

Figure 9. Simulated absorption spectrum for isomers derived from the crystal structure (DITAM, TIM-A, TIM-D, DITIM). Absorption maximum λ_{max} for Q- and Soret-bands are shown.

Figure 10. HOMO and LUMO isosurfaces for all stationary points. Letters H and L stand for HOMO and LUMO.

Table 1. Gas phase electronic energies and Gibbs free energies for the isomerization of DITAM. Coupled-cluster energies were computed at the DLPNO-CCSD(T)/cc-pVTZ level of theory. All energies are reported in kcal mol^{-1}

	uncatalyzed reaction path			
Environment	$\Delta G_1^{\ddagger}$	$\Delta G_2^{\ddagger}$	$\Delta G_3^{\ddagger}$	$\Delta G_4^{\ddagger}$
gas phase[a]	45.9	53.7	45.0	52.5
protein (ε=4.00)	38.9	45.7	40.5	47.1
	water-assisted path			
Environment	$\Delta G_1^{\ddagger}$	$\Delta G_2^{\ddagger}$	$\Delta G_3^{\ddagger}$	$\Delta G_4^{\ddagger}$
gas phase[b]	18.8	21.1	18.6	21.4
protein (ε=4.00)	12.9	20.3	13.1	17.3

[a,b] electronic energies only

Table 2. Absorption maximum λ_{max}, oscillator strength, and monoexcitations for the Q-band for all tautomers computed by optimizing the structure (opt) and using the backbone of the crystal structure (see Computational Details Section).

System	Excited state	λ_{max} (nm) (E_t in eV)	f (au)	Monoexcitations and CI coefficients
DITAM (crystal)	S_1	735 (1.69)	0.916	HOMO→LUMO (0.71)
DITAM (opt)	S_1	662 (1.87)	1.205	HOMO→LUMO (0.71)
TIM-A (crystal)	S_1	751 (1.65)	0.861	HOMO→LUMO (0.71)
TIM-A (opt)	S_1	658 (1.89)	1.164	HOMO→LUMO (0.71)
TIM-D (crystal)	S_2	728 (1.73)	0.738	HOMO→LUMO (0.60)
TIM-D (opt)	S_1	640 (1.94)	1.189	HOMO→LUMO (0.71)
DITIM (crystal)	S_1	757 (1.64)	0.820	HOMO→LUMO (0.71)
DITIM (opt)	S_1	645 (1.92)	1.111	HOMO→LUMO (0.71)

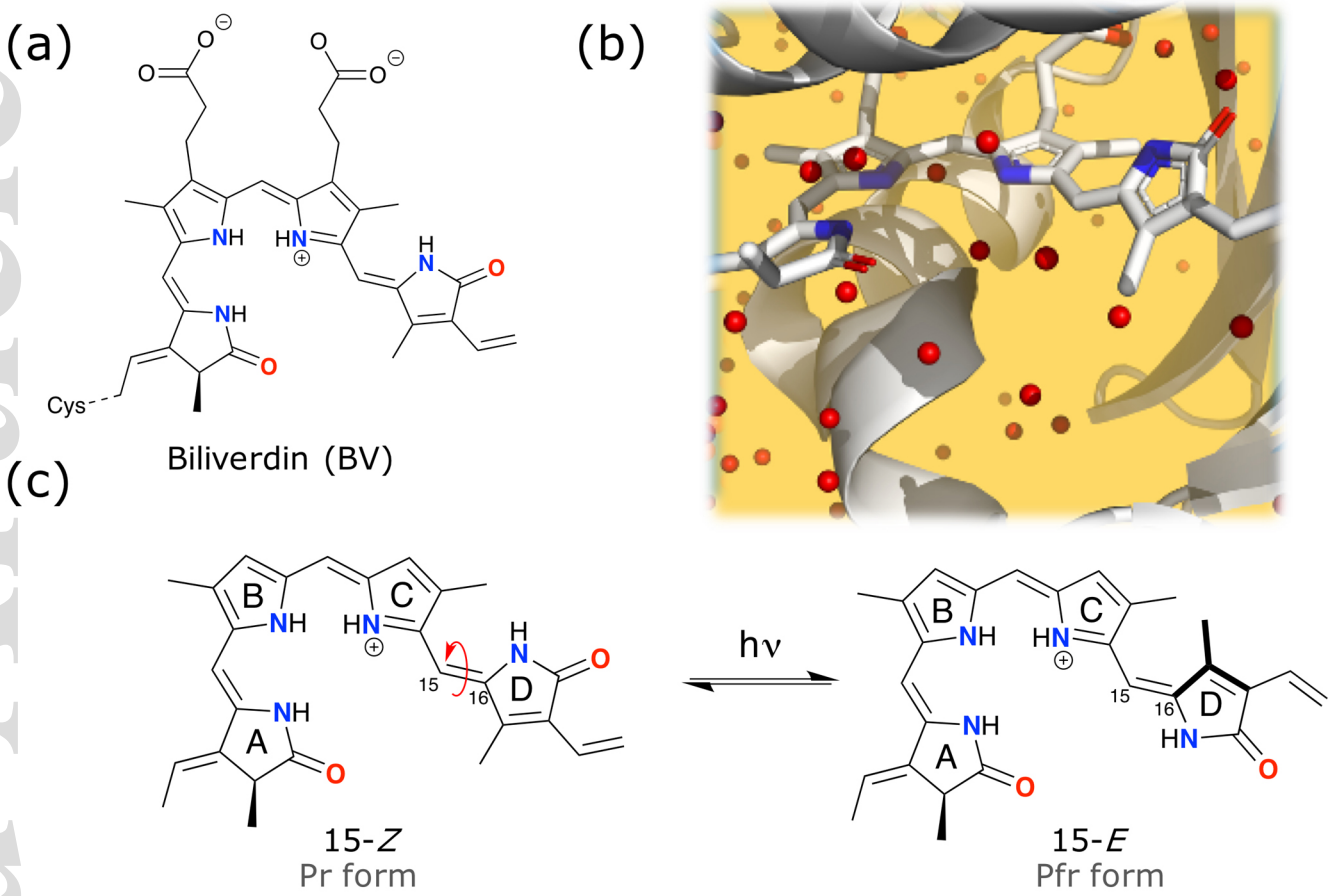

php_13341_f1.jpg

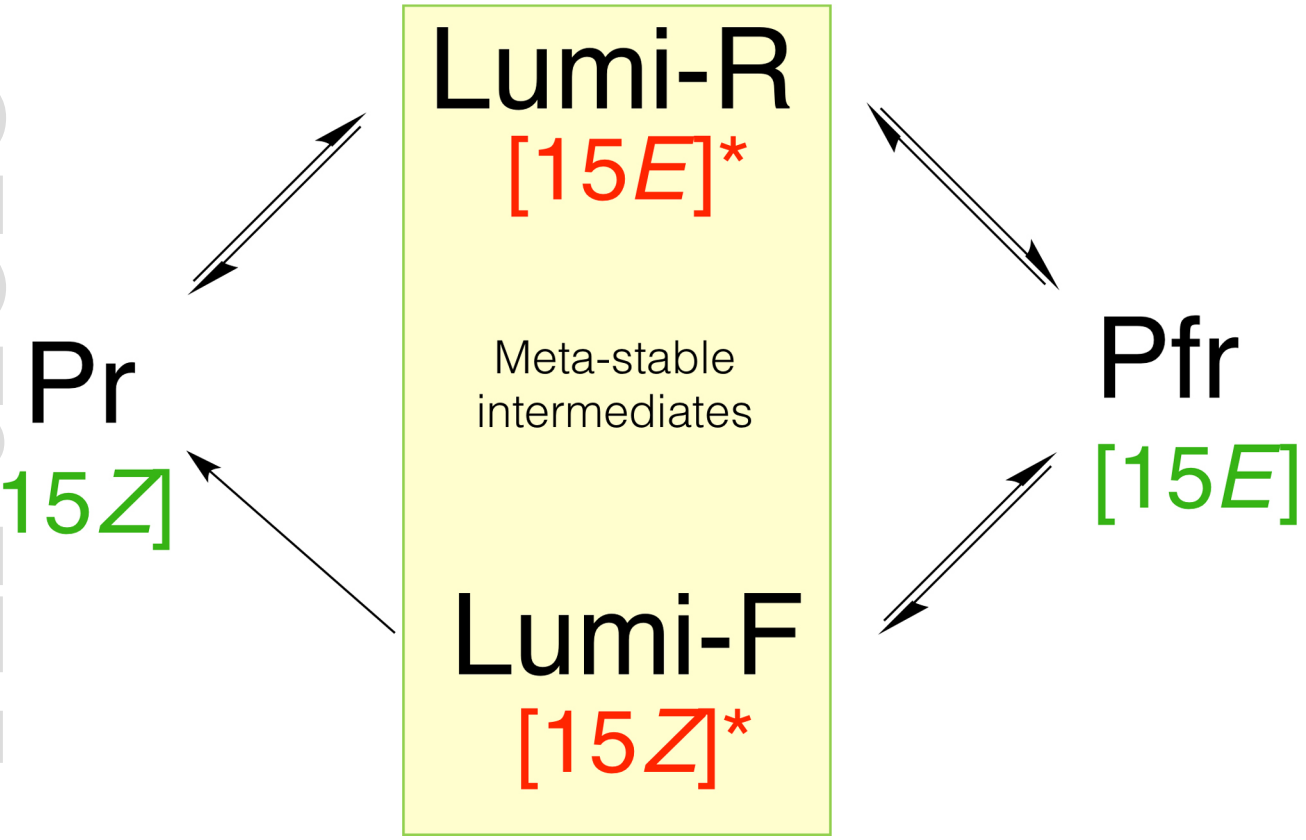

php_13341_f2.jpg

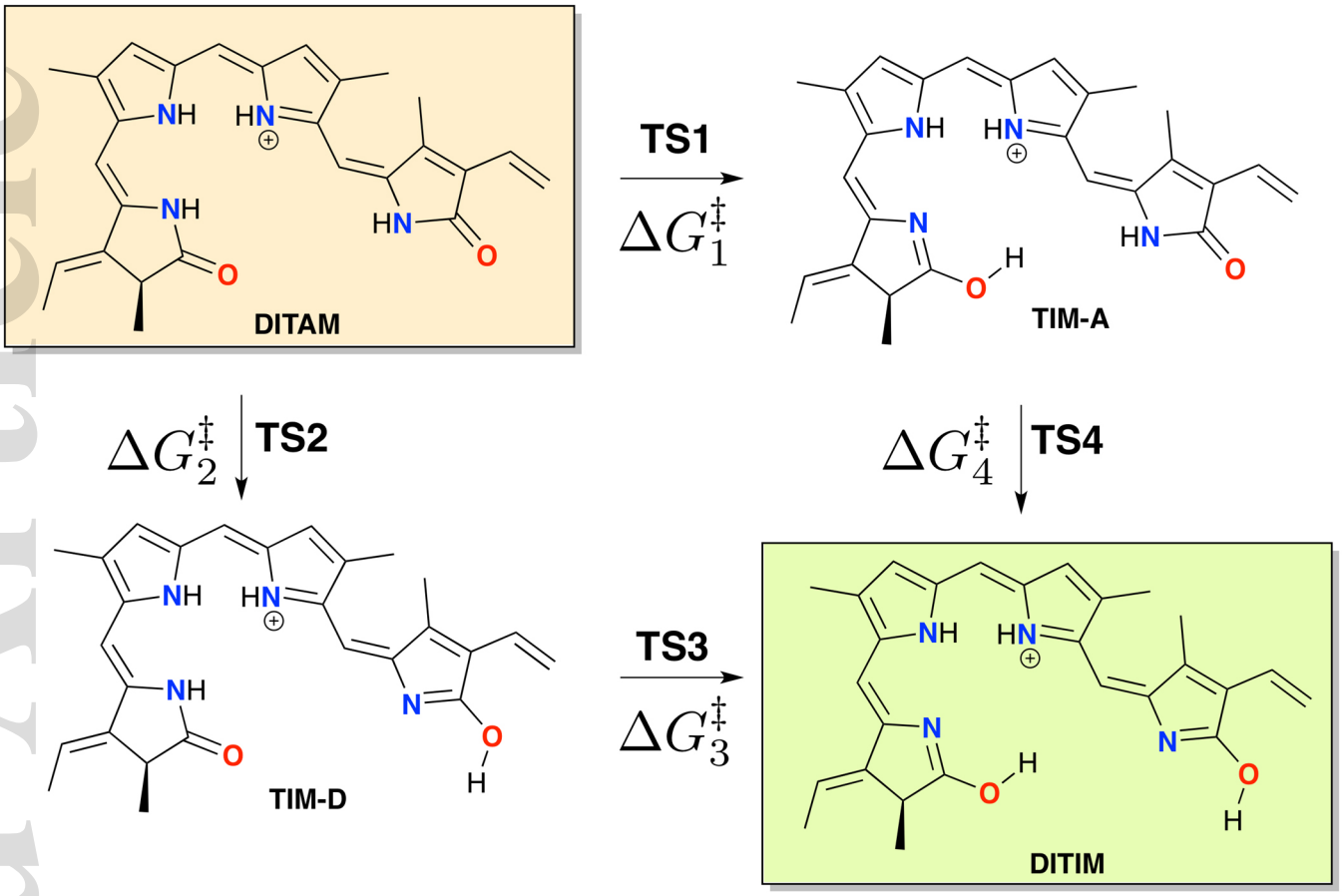

php_13341_f3.jpg

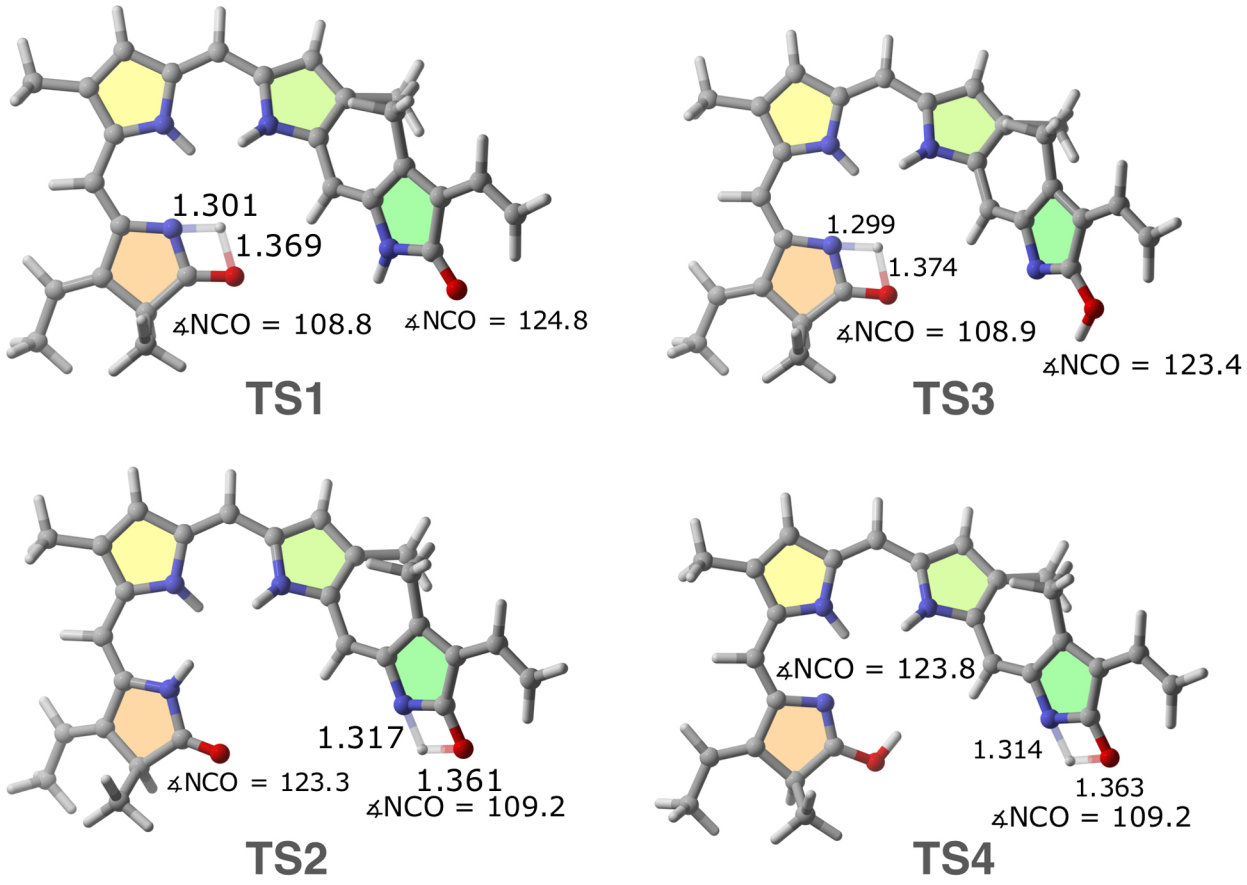

php_13341_f4.jpg

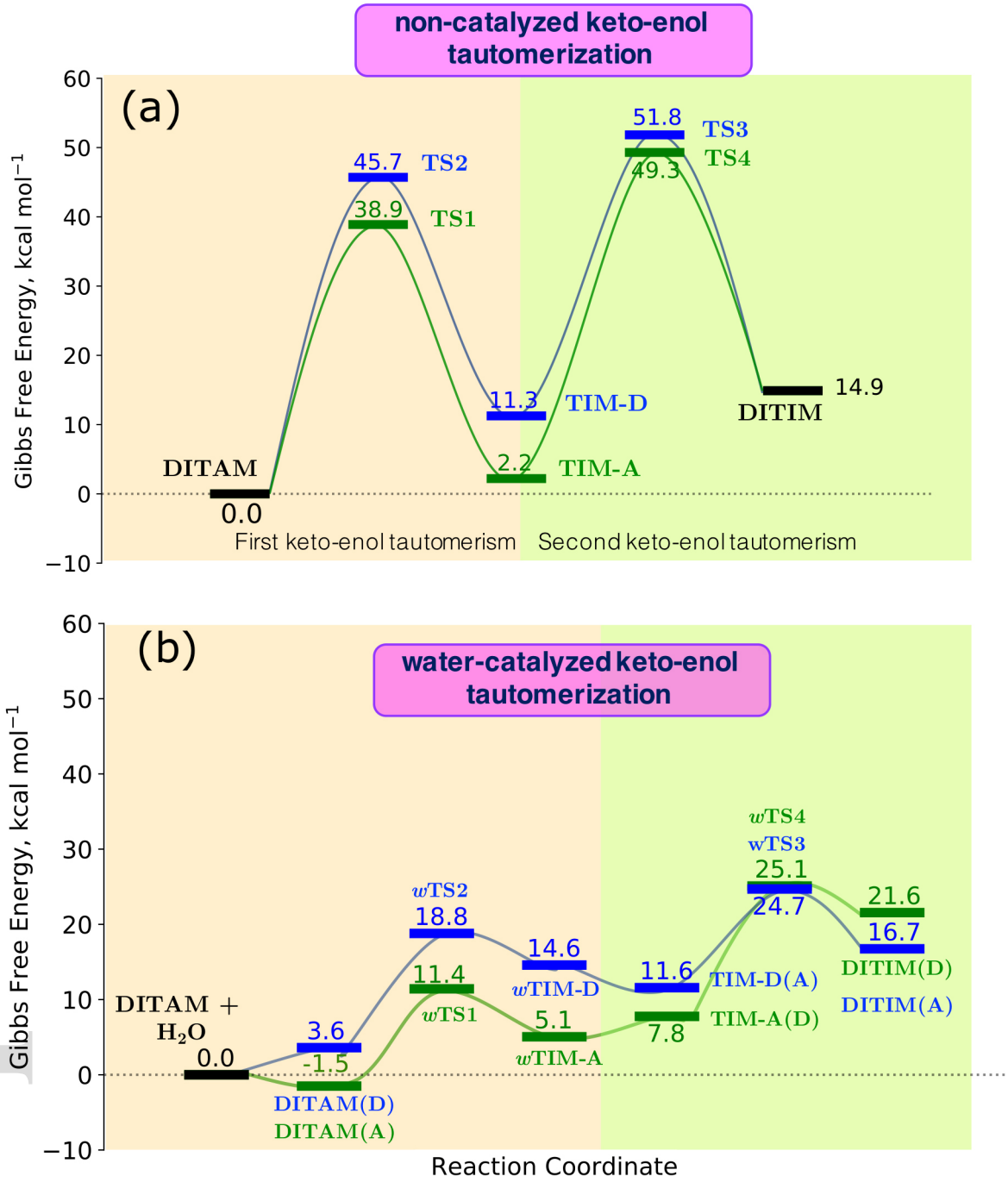

php_13341_f5.jpg

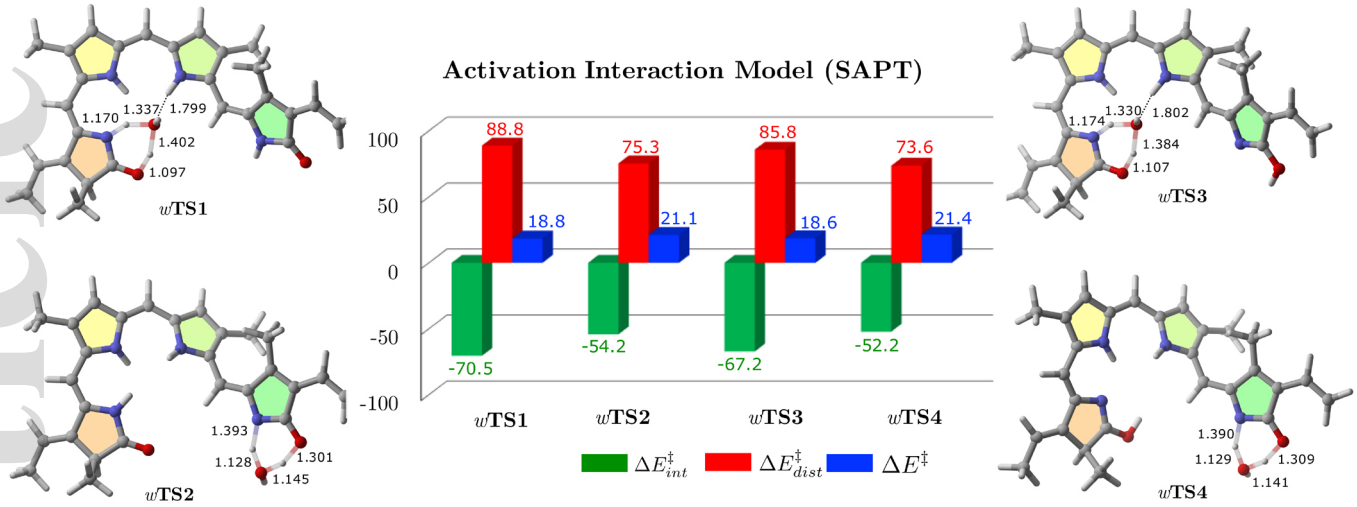

php_13341_f6.jpg

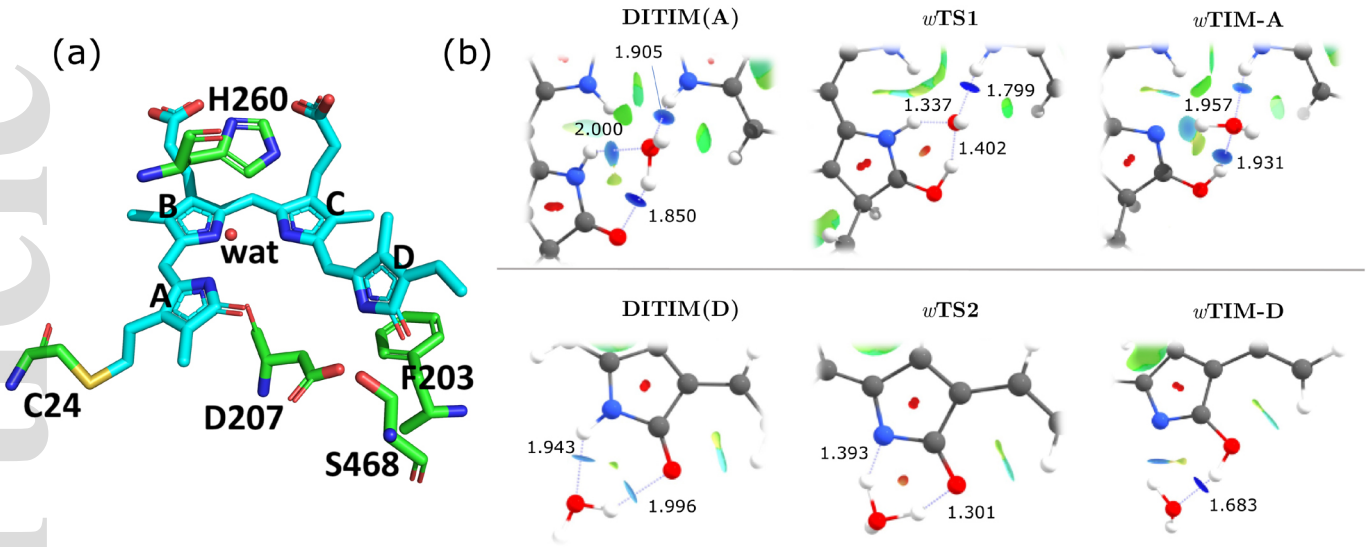

php_13341_f7.jpg

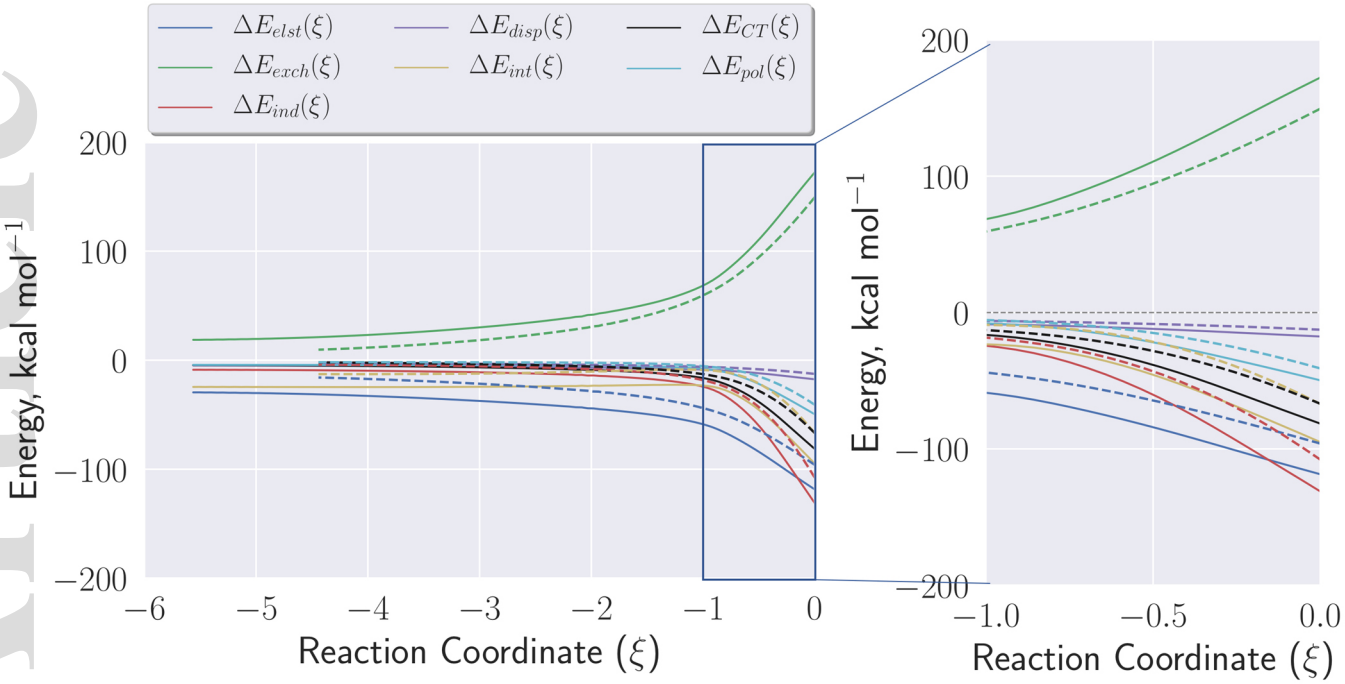

php_13341_f8.jpg

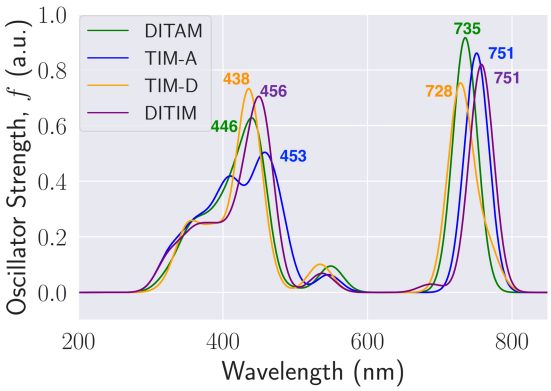

php_13341_f9.jpg

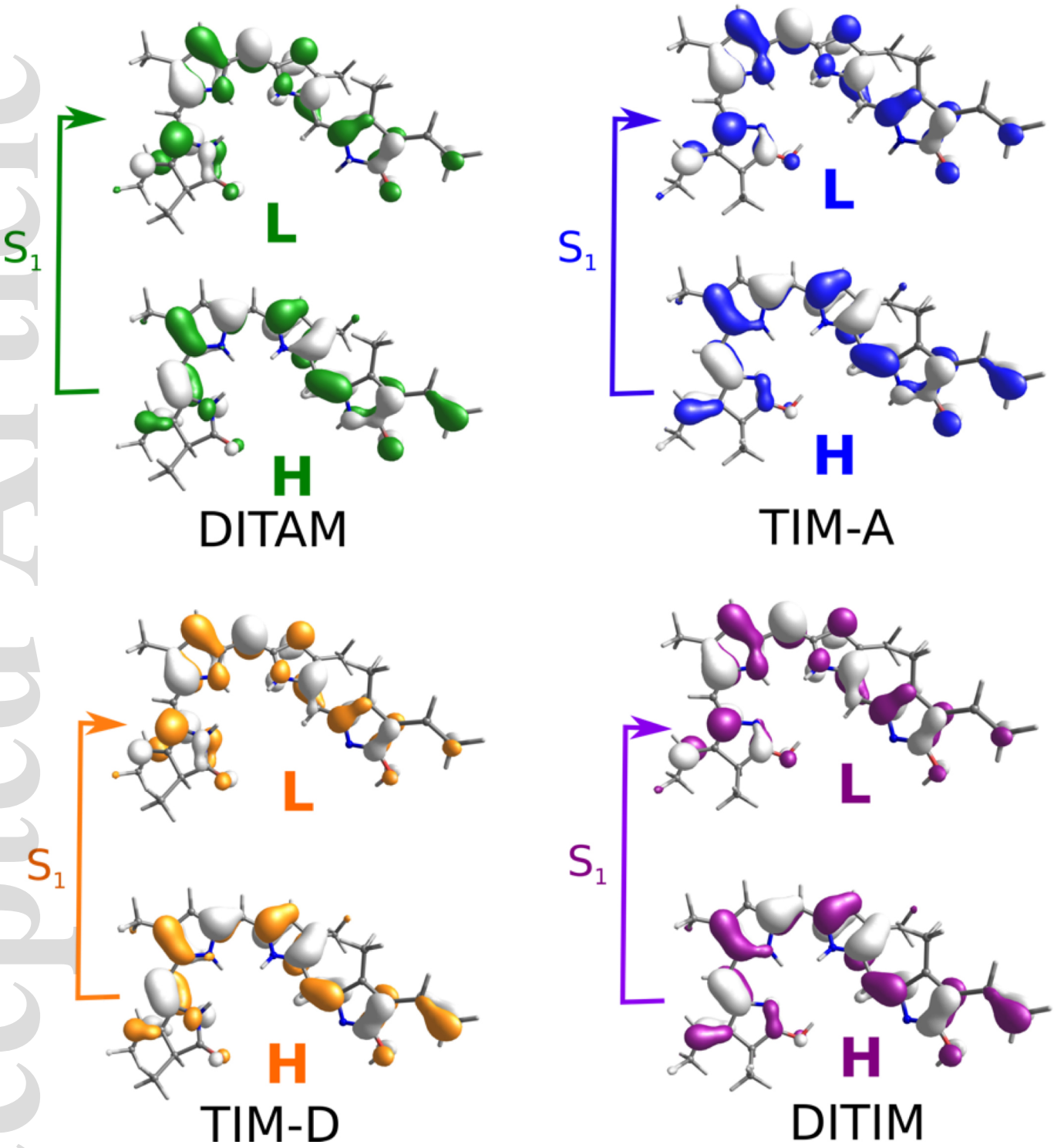

php_13341_f10.jpg